Dry powders reflectance model based on enhanced backscattering: case of hematite α–Fe2O3

Morgane Gerardin, Pauline Martinetto, Nicolas Holzschuch

Dry powders reflectance model based on enhanced back-scattering: case of hematite $\alpha - Fe_2O_3$

MORGANE GERARDIN,[1,2,*] PAULINE MARTINETTO,[2] AND NICOLAS HOLZSCHUCH[1]

[1] *Univ. Grenoble Alpes, CNRS, Inria, Grenoble INP, LJK, 38000 Grenoble, France*
[2] *Univ. Grenoble Alpes, CNRS, Institut Néel, 38000 Grenoble, France*
[*] *gerardin.morgane@gmail.com*

Abstract: By performing Bidirectionnal Reflectance Distribution Function (BRDF) measurements, we have identified back-scattering as the main phenomena involved in the appearance of dry nano-crystallized powders. We have developed an analytical and physically based BRDF model which relies on the enhanced back-scattering theory to accurately reproduce the measurements performed on optically thick layer of dry powders with various grains' morphology. Our results are significantly better than the ones obtained with previously existing models. The model has been validated against the BRDF measurements of multiple synthesized nano-crystallized and mono-disperse $\alpha - Fe_2O_3$ hematite powders. We also discuss the ability of our model to be extended to other material or more complex powder morphology.

1. Introduction

Accurate reproduction of powdered material appearance is an important issue in many domains such as environmental sciences, teledetection, digital prototyping, entertainment and art preservation. Powder materials are ubiquitous in real life, either used with a binder like pigments in most painting techniques and in some cosmetics such as lipstick, or dry such as spices, dry soils, dust, and pigments. The latter are particularly important as they are involved in parietal paintings from paleolithic to neolithic era. Some of them have been subject to many degradations processes to the point of becoming almost illegible. The digital reproduction of such cultural heritage artifacts through photo-realistic images synthesis will be of great interest for their preservation and will promote their broadcasting to a large audience.

Their appearance and more specifically the color of a powder material depends on both its chemical composition and on its morphometry, which refers to the size and the shape of its grains. This hypothesis is well known and particularly well justified in the case of pure $\alpha - Fe_2O_3$ hematite powders that can show various shades going from light red to purple [1,2]. The chemical composition of the material is involved in the absorption phenomena, while the morphology of the grains influences the way light is scattered by the material. Such light/matter interactions at the nanometric scale result in the macroscopic material appearance an observer perceive.

The light scattering by a material is numerically described using a *Bidirectional Scattering Distribution Function* (BSDF) model. Most of them assume that the light is mainly scattered at the surface of an object, around the specular direction that is to say in the direction opposite to the incident direction. Depending on the roughness of the surface, a more or less diffuse look is obtained. These models are not suitable in the case of dry powders for two reasons. First, powders are a medium composed of a collection of randomly oriented scatterers, so light is scattered multiple times in the volume of the medium, which is not taken into account by the surface models. To overcome this issue, one may use the Mie scattering theory [3]. This is relevant for powders diluted into a binder, and takes into account volume scattering depending on

the size and shape of the grains. But in the absence of a binder the grains composing the powder are too close to each other to actually be modeled using such model [2]. The second issue is that surface scattering models do not account for any scattering in the backward direction.

In this paper, we show that contrary to the prediction of most BSDF models the major contribution to a dry powder BSDF is not the specular peak but the back-scattering peak. We propose an analytical and physically-based BSDF model involving six parameters able to simulate the appearance of optically thick layer of dried pigments. We separate the model into two independent contributions: volume scattering and surface scattering. The former decomposes into single scattering and multiple scattering responsible for the sharp back-scattering lobe while the latter accounts for the specular scattering. This model has been developed and experimentally validated for seven hematite $\alpha - Fe_2O_3$ powders of different morphology. Our model reproduces the color variations of the studied samples, and can be applied to other pigments.
In Section 2 we will review previous works on BSDF models suitable for the description of dry powder materials, and more particularly on models that take into account the back-scattering contribution. The theoretical background necessary for the modeling of light scattering in a particle medium is introduced in Section 3. The $\alpha - Fe_2O_3$ samples and their measurements are described in Section 4. The description of our appearance model is done on Section 5 while in Section 6 we present its results, showing that it fits well the experimental BRDF of the studied samples. We conclude and give some future work directions in Section 7.

2. Previous work

Most of the BSDF models that are used in physically based renderers assume that the light is mainly scattered at the surface of an object, and in the specular direction which is to say the direction opposite to the incident direction. According to these models, the color of the rendered materials only depends on their chemical composition through the optical constants. In the case of participating media, the appearance also depends on physical properties and more particularly on the morphology of the involved scatterers. For diluted media, this is well described by the Lorenz-Mie scattering theory [3, 4].

Dry powders and pigments are even complex materials composed of a quite dense collection of particles with nanometric to micrometric grains' size. In the absence of a binder, the dry grains are too close to each other to be modeled using Mie scattering theory [2]. Their appearance is the result of absorption and scattering phenomena, so its description suggests the full understanding of the interactions of light with the material at both its surface and in its volume.

The incoming light is partially scattered at the surface of the material. This phenomenon can be empirically modeled using the microfacet model [5] by considering that the surface is made of small but larger than wavelength specular micro facets with known orientations distribution. Alternatively, the generalized Harvey-Shack theory [6] allows to predict the reflectance of a rough surface while taking into account the diffraction effects caused by surface asperities. It accurately simulates the appearance of opaque and homogeneous materials but only considers single scattering.

As we will show in this paper, in the case of pigments an important amount of the incoming light is scattered backwards, responsible for a high peak back into the incident direction. This scattering phenomena, known as *back-scattering*, has already be observed on other dry powders such as meteorites soils [7], and has already been taken into account in some BRDF models: the spectralon model, the RTLSR model and the enhanced back-scattering model.

2.1. Spectralon

An empirical one has been developed by [8] to model the BRDF of the Spectralon®, a material that resembles a powder since it is made out of a collection of compressed polymer particles.

This model is assumed to be the summation of four independent scattering phenomena, occurring at both the surface and in the volume of the material. As it involves a large number of material-dependent parameters optimized in the specific case of Spectralon, it can be adapted to reproduce with a high fidelity a large range of materials. Nevertheless, these parameters has no explicit relationship with the chemical composition nor the physical parameters of the considered material so they cannot be predicted, but only deduced from measurement fittings.

2.2. RTLSR

The RTLSR (Ross-Thick Li-Sparse Reflectance) model [9, 10], is a semi-empirical model used in teledetection for simulating the BRDF of forest canopies. It decomposes the BRDF into a volume scattering contribution deduced from an approximation of the radiative transfer theory (RT) [11], and surface scattering which is inferred according to purely geometrical considerations [12]. An optimization factor allows to control the proportion of each of the contributions. Initially developed for thick and sparse canopies, extensions of this model have been proposed for thin and dense media [13]. [14] brought modifications to the model for the study of snow, and multiple works [12, 15, 16] agree that it can be used for bare soils although they do not explicitly introduce the changes that should be done in such a case. Because of its unique controllable parameter, this model is too rigid and remains unable to reproduce fine appearance variations.

2.3. Enhanced Back-scattering

A deeper analysis of the back-scattering phenomena (see Section 3.5) occurring in a scattering medium refers to *Enhanced Back-Scattering (EBS)*, which describes it as the result of constructive interferences [17], [18]. Contrary to the RT theory, the scattered fields are supposed to be correlated. As a result, the EBS is the sum of the two terms of RT theory (*single* and *multiple scattering*) and a third one accounting for the constructive interferences in the backward direction. As the analytical results are deduced within the diffusion approximation, only isotropic particles are considered. Nevertheless, [17] extended the model to account for anisotropic scattering in the case of normal incidence.

3. Background

As a dry powder layer involves a large number of scatterers with relatively high density, it is complex to describe the scattering of light in such a medium. Most of the time, it can be done using the radiative transfer theory (RT) [19], [20], which accounts for both single and multiple scattering inside the medium. As it relies on the assumption that the scattered fields are uncorrelated, RT is unable to predict the appearance of materials which exhibits a strong back-scattering contribution. In this section, let's overview the theoretical aspects and hypotheses useful for an extension of RT known as the enhanced back scattering theory (EBS), that takes into account correlated scattered fields to describe the back-scattering phenomenon.

3.1. Medium description

Let's consider a region 0 free of scatterers with wavenumber $k_0 = 2\pi/\lambda$, and a medium 1 characterized by an effective wavenumber $K = K' + iK''$ containing $\mathcal{N}$ scattering spherical inclusions per unit volume. All scatterers have the same radius r and scattering properties (Figure 1).

The medium is illuminated in the incoming direction θ_i by the light coming from a point source at the position $\boldsymbol{r_i}$ in the region 0. The light scattered by the slab is observed at a point in region 0 in the direction (θ_o,φ) at a distance $r_o >> 1$ from the interface. To ease the description of the scattering inside the layer, point scatterer approximation is made: the scattering events occur a the center point of the spherical scatterers.

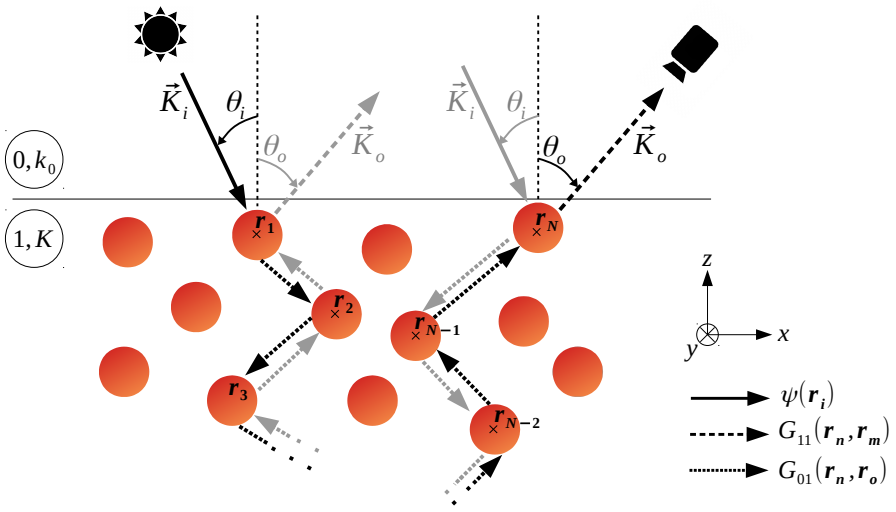

Fig. 1. N-th order multiple scattering in a medium composed of particles. The incident ray follows a path going from the particle at $\boldsymbol{r_1}$ to the one at $\boldsymbol{r_N}$. Interferences occur with the ray from $\boldsymbol{r_N}$ to $\boldsymbol{r_1}$. The incoherent part of the resulting field (denoted as $\mathcal{L}_N$ in Section 5.1) contributes to the ladder term while its coherent part (denoted as C_N in Section 5.1) accounts for the cyclical term.

3.2. Foldy's approximation

For a sufficiently small density of scatterers, the effective wavenumber K can be expressed using the Foldy's approximation [21]:

$$K \approx k_0 + \mathrm{i}\frac{2\pi\mathcal{N}}{k_0}F \tag{1}$$

where F is the complex scattering amplitude, describing the scattering properties of the particles.

3.3. Light propagation

The propagation of light inside a medium containing scattering particles is illustrated by the Figure 1. The light ray coming from region 0 without being scattered is described by the incident field :

$$\psi_m(r_i) = \exp(\mathrm{i}\boldsymbol{K_i} \cdot \boldsymbol{r_i}) \tag{2}$$

where $\boldsymbol{K_i}$ is of magnitude K given by the Foldy's approximation, and oriented in the incident direction.

After it has been scattered by a particle, light travels in the region 1 towards another scatterer, as if it was in a space free of scatterer. Under this hypothesis, the propagation of light from a position $\boldsymbol{r'}$ towards $\boldsymbol{r}$ is given by the Green's function $G(\boldsymbol{r}, \boldsymbol{r'})$, that satisfies the Helmholtz equation :

$$(\Delta + k^2)G(\boldsymbol{r}, \boldsymbol{r'}) = \delta(r - r') \tag{3}$$

By averaging over the particles, the mean Green's function referring to the propagation of light from an inclusion to another is given as follows:

$$G_{11}(\boldsymbol{r_n}, \boldsymbol{r_m}) = \frac{\exp(\mathrm{i}\boldsymbol{K} \cdot |\boldsymbol{r_n} - \boldsymbol{r_m}|)}{4\pi|\boldsymbol{r_n} - \boldsymbol{r_m}|} \tag{4}$$

where $\boldsymbol{r_m}$ and $\boldsymbol{r_n}$ are the positions of two distinct scatterers in the medium 1. In the same way,

$$G_{01}(\boldsymbol{r_n}, \boldsymbol{r_o}) = \frac{\exp(\mathrm{i}k_0 r_o)}{4\pi r_o} \exp(-\mathrm{i}\boldsymbol{K_o} \cdot \boldsymbol{r_n}) \tag{5}$$

describes the propagation from a scatterer at position $\boldsymbol{r_n}$ in region 1 towards the camera at $\boldsymbol{r_o}$ in region 0. The vector $\boldsymbol{K_o}$ is of magnitude K and oriented towards the camera.

3.4. Light scattering by one particle

The scattering events caused by the encountering of light with the n-th scatterer is described using the transition operator T_n that we introduced as :

$$T_n(\boldsymbol{r_n}) = 4\pi F(\Theta_n)\delta(r_{in} - r_{on}) = 4\pi F(\Theta_n) \tag{6}$$

where $\Theta_n = \theta_{on} - \theta_{in}$ is the scattering angle between the incident direction on the n-th scatterer θ_{in} and the outgoing direction θ_{on}.

The complex scattering amplitude $F(\Theta_n)$ is linked to the scattering phase fucntion using the relationship:

$$\rho p(\Theta_n) = \frac{4\pi N}{\kappa} |F(\Theta_n)|^2 \tag{7}$$

where ρ is the single scattering albedo and κ the extinction rate.

3.5. Enhanced back-scattering

The EBS theory offers a physical description of the back scattering phenomenon observed in quite dense media. It is an extension of radiative transfer (RT) theory [19], [20]: the so called *ladder terms* accounting for both single scattering $BRDF_{ebs,\mathcal{L}_1}$ and some multiple scattering $BRDF_{ebs,\mathcal{L}_{2+}}$ takes into account the contribution of uncorrelated scattered fields already described by the RT theory. This model also accounts for coherent scattered fields that induce interference effects as light undergoes multiple scattering events in the medium. It is described by a *cyclical term* $BRDF_{ebs,C}$ and results in a sharp peak in the back-scattering direction.

The BRDF is then composed of three contributions:

$$BRDF_{ebs} = BRDF_{ebs,\mathcal{L}_1} + BRDF_{ebs,\mathcal{L}_{2+}} + BRDF_{ebs,C} \tag{8}$$

This model has been developed for thick layers of a medium composed of isotropic spherical scatterers of radius r with a constant phase function $p(\Theta) = p$ embedded in a host medium [17, 18, 22, 23].

Analytical expressions of the multiple scattering terms are obtained by considering that for optically thick media with high albedo the resulting overall scattering statistically tends to be isotropic. This is known as the *diffusion approximation* and leads to results in Eqs. 9.

$$\begin{cases} BRDF_{ebs,\mathcal{L}_1} = \dfrac{\rho p(\Theta)}{\mu_o + \mu_i}\left[1 - \exp\left(-\kappa d\left(\dfrac{1}{\mu_o} + \dfrac{1}{\mu_i}\right)\right)\right] & \text{(9a)} \\ BRDF_{ebs,\mathcal{L}_{2+}} = \dfrac{3\rho^2}{1 - \mu_i^2 c^2}\left[\dfrac{2Q}{1 - \mu_o c} - \dfrac{\mu_i^2}{\mu_i + \mu_o}\right] & \text{(9b)} \\ BRDF_{ebs,C} = \dfrac{3\rho^2[c + v(1 - \exp(-2c\tau_o))]}{2\mu_i\mu_o c v[(c+v)^2 + u^2]} & \text{(9c)} \end{cases}$$

The parameters u, v, c and Q in Eqs. 9 vary with the isotropy of the scatterers and with the geometry under which the medium is illuminated and observed. It has been described by [18] for

isotropic scatterers such as:

$$
\begin{cases}
u = \dfrac{k_0}{\kappa}(\mu_i - \mu_o) & \text{(10a)} \\
v = \dfrac{1}{2}\left(\dfrac{1}{\mu_i} + \dfrac{1}{\mu_o}\right) & \text{(10b)} \\
\alpha = \dfrac{k_0}{\kappa} f & \text{(10c)} \\
\kappa_{tr} = 1 - \rho & \text{(10d)} \\
c = \sqrt{3(1-\rho)\kappa_{tr} + \alpha^2} & \text{(10e)} \\
Q = \dfrac{[1 + \mu_i c - (1 - \mu_i c)\exp(-2c\tau_o)]}{4c} & \text{(10f)}
\end{cases}
$$

where f is the norm of the vector $\boldsymbol{f}$ defined as difference between the projections of the normalized incoming and outgoing direction vectors (Figure 2) which allows the BRDF modelization in any azimuthal plane.

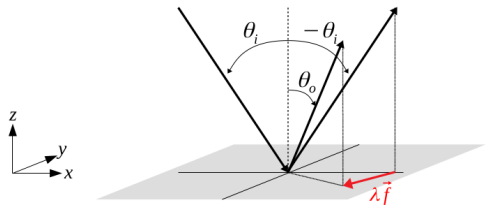

Fig. 2. Definition of the vector **f**.

Only the single scattering term involves the phase function in such a case. [17] introduce the consideration of anisotropic scatterers but only with normal incidence. We will discuss the extension of the model for anisotropic scattering in the Section 5.

The last parameter involved in the BRDF expressions (Eqs. 9) is the extinction ratio τ_o that is defined as intrinsic to the scatterers' material. It accounts for internal reflections that may occur between the interface of the medium. A definition is given by [24]:

$$\tau_o = \frac{2}{3}\frac{1 - \bar{R}}{1 + \bar{R}} \tag{11}$$

with $\bar{R} = \dfrac{3C_2 + 2C_1}{3C_2 - 2C_1 + 2}$ and $C_i = \displaystyle\int_0^{\frac{\pi}{2}} R(\theta)\cos^i\theta\sin\theta \mathrm{d}\theta$

In the previous equations, $R(\theta)$ is the Fresnel's angular reflection coefficient [25]. The parameter τ_o thereby depends on the optical constants of the material the particles are made of and on the wavelength.

4. Sample description and BRDF measurements

The physical phenomena at stake in the appearance of a material can be inferred through the BRDF measurement.

4.1. Sample description

For the study of dry powder appearance we focused on synthetic nano-crystallized hematite $\alpha - Fe_2O_3$ powders with various colors, that we obtained using different routes allowing to control the nucleation and growth of $\alpha - Fe_2O_3$ crystallites in solution. These samples are presented on Figure 3

The samples we have denoted from 1 to 5 have been prepared following methods described by [26]. 1, 2 and 5 have been obtained by forced hydrolysis of Fe^{III} salts solutions in acidic conditions, while 3 and 4 are the results of the transformation of a ferrihydrite precipitate in aqueous suspension under basic conditions. We generated peanuts-like hematite particles 6 following the routes proposed by [27], NaH_2PO_4 salts. Sample 7 is a commercial Iron(III) oxide powder sample purchased from Puratronic®.

The color and the morphometry of each sample are respectively deduced from naked eye observations completed with optical microscopy using a Nikon Eclipse LV100ND microscope, and by scanning electron microscopy observations performed with a Zeiss Ultra+ microscope. Various grains' shape and size ranging from 10 nm to 10 µm are obtained. The small grains are characterized by a lighter red color (samples 1 to 5) while a darker purple hue is observed for the pigments with larger grains (samples 6 and 7). We may also note that samples 5, 6 and 7 can be described by two grain sizes: either two different size populations (sample 5), either large grains that are agglomerates of smaller ones (samples 6 and 7).

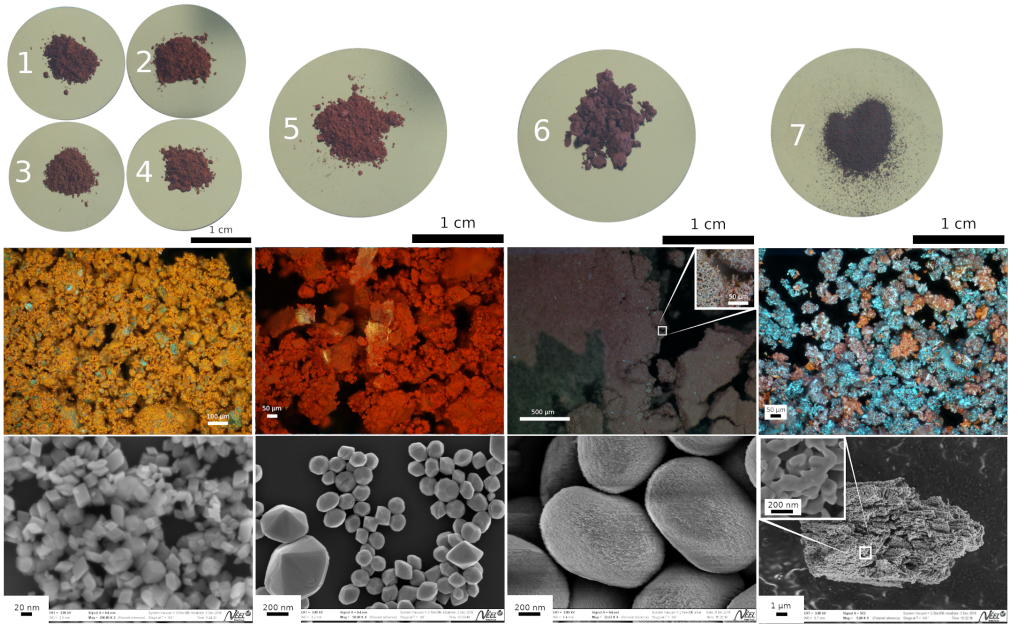

Fig. 3. $\alpha - Fe_2O_3$ hematite samples under study, showing various colors and grains' morphology. Upper row: The photographs are calibrated using an X-rite 24 patches Classic Colorchecker. Middle row: Observations using optical microscopy. Lower row: Samples' morphology observations using Scanning Electron Microscopy. The samples 1 to 4 show similar grain shape, with slightly different sizes from 10 to 50 nm in diameter, and light red hue. Sample 5 presents two size populations and shows a red-pinkish hue. Samples 6 and 7 have a more complex morphology with grains that seem to be agglomerations of smaller ones. The grains are larger and a darker purple hue is observed. According to optical microscopy, 7 is even composed of different types of grains, with different colors.

4.2. BRDF measurements

The whole BRDF of each sample is measured by combining two distinct measurements, depending on which scattering geometry is at stake. The first one does not account for the back-scattering, while the second one is specifically performed to account for this contribution.

4.2.1. Out the back-scattering

The main part of the BRDF is measured using the SHADOWS instrument [28], over 180 geometries: the scattered light is observed for $\theta_o \in [-70°, 70°]$, for incidences $\theta_i \in [\![0°, 20°, 40°, 60°]\!]$ and azimuthal angles $\varphi \in [\![0°, 30°, 60°, 90°]\!]$, and 135°. The spectral range has been limited to 360 nm - 860 nm with a step of 20 nm. The reflectance measurements are calibrated with a Spectralon. Every point is measured with an integration time of 300 ms and averaged over 10 spectra. Such measurement takes about 18 hours.

When it comes to a geometry where incident and observation directions are identical, the instrument's design causes the sensor to be obstructed by the light source. A specific device needs to be designed to evaluate the amount of light scattered in these directions.

4.2.2. In the back-scattering direction using an in-house-built set-up

Our design for measuring the back-scattering contribution to the BRDF is inspired from the work of [29] and [8]. As these only deal with vertically held samples, they cannot be used for studying dry powders. We propose a new design to allow the measurement of any horizontally held sample.

We chose an halogen light source to normally illuminate the sample after being reflected by a beam splitter at 45°. The size of the illumination spot is minimized by focusing the light with a 50 mm focal lens. An additional diaphragm is added to clean the focused beam. The direction of the incident light θ_i is adjusted by positioning the beam splitter at an angle of $45° + \theta_i/2$. As the light interacts with the powder, it is scattered in every directions and preferably back into the incident direction. It is then partially transmitted through the beam splitter and collected by a Thorlabs F950FC-A collimator. The latter is fixed on a vertical rotating plate so that we can scan different observation directions around the exact back-scattering one in the incident plane. We use a fiber spectrometer OceanOptics USB650 along with the SpectraSuite software in order to detect and visualize the measured signal.

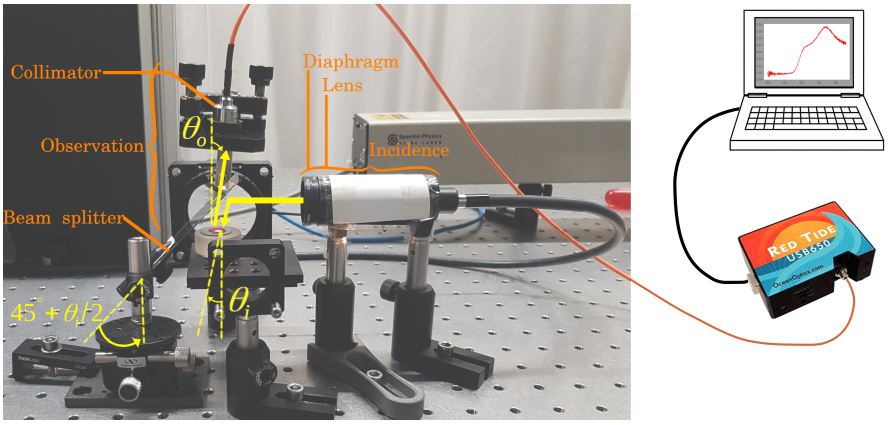

Fig. 4. Back-scattering measurement device. The beam of a white source is focused on the sample's surface at an incidence θ_i using a 50 mm focal lens and a beam splitter. The reflected light is collected through a collimator in different observation directions θ_o.

In the incident plane ($\varphi = 0°$), we scan the observation angles in the range $[\theta_i - 10°, \theta_i + 10°]$ with a step of 2°, for incidences 0°, 20° and 40°. The reflectance measurements are calibrated with a Spectralon. The integration time is chosen to maximize the detected signal and an averaging over 5 spectra is performed to minimize the noise. Less than 20 seconds in necessary to measure one spectrum.

4.2.3. Complete measurement

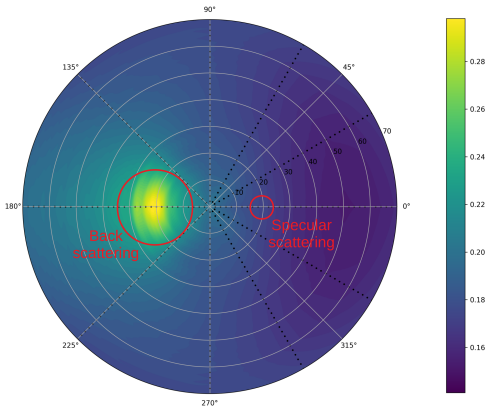

Fig. 5. Complete BRDF of the hematite powder sample 1 at the wavelength 700 nm for an incidence $\theta_i = 40°$. The measured geometries are spotted with black dots, and the intermediate values are interpolated. Light is mostly reflected in the backward direction, and a very weak specular scattering peak may be observed as well. The spreading of the back scattering peak with the azimuth angle is due to the colormap interpolation between the measured points.

As the two measurements are performed independently, they happen to be shifted in amplitude from one another. This may be caused by the underestimation of the back scattering of the spectralon used for photometric calibration. Since the difference is smaller than 5%, a re-scaling of the back-scattering measurement is done so it matches the goniometer results.

A typical experimental BRDF is shown figure 6 after merging the measured data. The measurements show that the BRDF of dry hematite powders is composed of an overall diffuse contribution, and two directional scattering phenomena including mainly back-scattering and some specular scattering (Figure 5). The BRDFs of characterized samples vary in intensity and width of the specularly and back scattered lobes. We give results for the six other samples under study in Supplementary Work.

5. Powder BRDF Model

As shown by the measurements on Figure 5, powders' BRDF mainly involves back-scattering and almost no specular scattering which makes the usual specular BRDF models ineffective to reproduce their appearance.

Although our model is derived from a study on pure nano-crystallized hematite powders, we chose a physically-based approach so that it can be applied to any other pigment. It involves both chemical composition and morphological parameters to accurately account for the color variations observed on such pigments. Moreover it allows to consider either isotropic or anisotropic scatterers. Inspired by both RTLSR and Spectralon's models, our model is divided

into two contributions respectively accounting for volume and surface scattering.

$$BRDF = A_v BRDF_v + A_s BRDF_s \tag{12}$$

These two contributions are weighted with the amplitude parameters A_v and A_s.
The main difference with the previously introduced models is that, based on the EBS theory the back scattering is considered as part of the volume contribution. The surface contribution is then reduced to specular scattering caused by surface roughness.

5.1. Volume scattering

As EBS theory is established within the diffusion approximation, the averaged scattering is assumed to be isotropic. This greatly simplifies the multiple scattering contribution by considering the scattering phase function as constant over the whole scattering hemisphere. The anisotropic scattering of each particle is accounted for by choosing the phase function parameter g involved in the single scattering contribution. The extension of the model for taking into account this anisotropy in multiple scattering has only been done for a normal incidence by Tsang et al. [17].

In the following we expose the calculations that we made in order to consider anisotropic scattering in both single and multiple scattering terms for any $\theta_i/(\theta_o, \varphi_o)$ geometry. The final model only involves two variable parameters (g, κ) that rely on the physical and chemical properties of the material that is under study.

First order ladder term $\mathcal{L}_1$: This contribution accounts for light that is only scattered once before being observed and is similar to the one introduce in Section 3.5. The anisotropy is taking care of by the scattering phase function involved in the analytical expression of $BRDF_{ebs,\mathcal{L}_1}$ in Eq. 9.

Multiple ladder term $\mathcal{L}_{2+}$: The phase function is involved at every scattering event that light encounters as it travels the particulate medium. We denote P_i and P_o respectively the first and the last particles that are responsible for light scattering along a light path.

At the second scattering order, the light is first incoming on P_i, scattered with an angle Θ_i towards the particle P_o, and finally scattered towards the observer with an angle Θ_o as illustrated by the Figure 6.

For the $n-$th scattering order, light undergoes n scattering events. As for the second order, it undergoes a first one described by the angle Θ_i while encountering the particle P_i and last one with the particle P_o and the angle Θ_o. But it also interacts with $n-2$ other particles in between, resulting in $n-2$ scattering events respectively described by the scattering angles $\Theta_k = \theta_{ik} - \theta_{ok}$, difference between the incoming direction θ_{ik} and outgoing direction θ_{ok} on the $k-$th particle, with $k = [\![2\ ;\ \infty]\!]$ as it is shown on the Figure 6.

By averaging over all the possible paths that light can follow inside the medium while encountering n scatterers, we can write the $n-$th order ladder term as follows:

$$\begin{aligned}\mathcal{L}_n =& \frac{(4\pi)^{n-2}(\rho\kappa)^n}{r^2} \\ &\times \int |p(\Theta_n)|^2 |G_{11}(\boldsymbol{r_n}, \boldsymbol{r_{n-1}})|^2 ... |G_{11}(\boldsymbol{r_2}, \boldsymbol{r_1})|^2 |p(\Theta_1)|^2 \exp\left(\kappa\left(\frac{z_1}{\mu_o} + \frac{z_n}{\mu_i}\right)\right) \mathrm{d}\boldsymbol{r_1} ... \mathrm{d}\boldsymbol{r_n}\end{aligned} \tag{13}$$

with r the distance from the sample to the observation point.

The total ladder term accounting for multiple scattering can be written in a recursive way, giving:

$$\mathcal{L}_{2+} = \int\int \exp(\kappa(\frac{z_i}{\mu_o} + \frac{z_o}{\mu_i}) A(\boldsymbol{r_i}, \boldsymbol{r_o}) \mathrm{d}\boldsymbol{r_i} \mathrm{d}\boldsymbol{r_o} \tag{14}$$

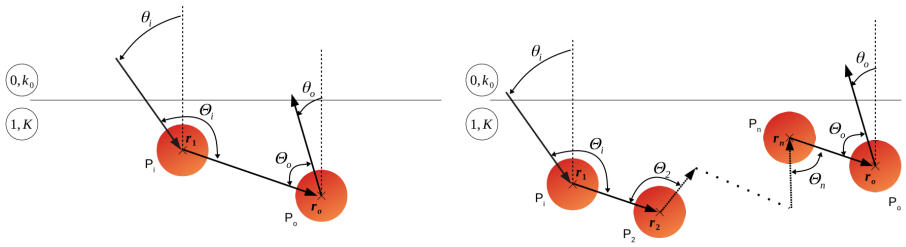

(a) Scattering with two particles (b) Scattering with n particles

Fig. 6. Mutliple scattering with two and n particles. The first scatterer that light encounters as it travels inside the medium is denoted as P_i and involves a scattering event described by the angle Θ_i. The last scattering event before light goes out of the medium is caused by the scatterer P_o with an angle Θ_o. In between these two scatterers, light is scattered with an angle Θ_k at each interaction with a particle k.

with $A(\boldsymbol{r_i}, \boldsymbol{r_o})$ defined such as:

$$A(\boldsymbol{r_i}, \boldsymbol{r_o}) = \left(\frac{\rho\kappa}{4\pi}\right)^2 p(\Theta_1)p(\Theta_o)\frac{\exp(\kappa|\boldsymbol{r_i} - \boldsymbol{r_o}|)}{|\boldsymbol{r_i} - \boldsymbol{r_o}|^2} + \int \left(\frac{\rho\kappa}{4\pi}\right) p(\Theta_n)\frac{\exp(\kappa|\boldsymbol{r_i} - \boldsymbol{r_n}|)}{|\boldsymbol{r_i} - \boldsymbol{r_n}|^2} A(\boldsymbol{r_n}, \boldsymbol{r_o})\mathrm{d}\boldsymbol{r_n} \tag{15}$$

Note that contrary to the ladder term defined by the Eq. 9, our model involves a varying scattering phase function whose expression is chosen to better model the material under study. If one wants to describe isotropic scattering a constant phase function such as $p(\Theta) = p$ should be used which leads back to the expression originally introduced in Section 3.5.

The resulting BRDF of the ladder contribution is then given by:

$$BRDF_{\mathcal{L}_{2+}} = \frac{4\pi r^2 \mathcal{L}_{2+}}{a\mu_i\mu_o} \tag{16}$$

where a is the area of the sample under studied.

Multiple cyclical scattering C: As for the ladder term, we are aiming to take into account the anisotropic scattering of particles in the cyclical term. We will use the same assumptions as illustrated by the Figure 6. We consider a ray of light that is scattered by n particles as it follows a path inside the medium. By accounting for the correlation between this path and its reversal and averaging over all the possible paths, the $n-$th order cyclical term can be written:

$$\begin{aligned} C_n = &\frac{(4\pi)^{n-2}(\rho\kappa)^n}{r^2}\int |p(\Theta_n)|^2 |G_{11}(\boldsymbol{r_n}, \boldsymbol{r_{n-1}})|^2 ... |G_{11}(\boldsymbol{r_2}, \boldsymbol{r_1})|^2 |p(\Theta_1)|^2 \\ &\times \cos\left(k(\mu_i - \mu_o)(z_1 - z_n)\right)\exp\left(\frac{\kappa}{2}\left(\frac{1}{\mu_o} + \frac{1}{\mu_i}\right)(z_1 + z_n)\right)\mathrm{d}\boldsymbol{r_1}...\mathrm{d}\boldsymbol{r_n} \end{aligned} \tag{17}$$

The complete cyclical contribution is obtained by summing over the $n-$th orders and can be simplified replacing G_{11} by its definition (Eqs. 4). By using the new expression of $A(\boldsymbol{r_i}, \boldsymbol{r_o})$ given by Eq. 15:

$$C = \int\int \cos(2k(\mu_i - \mu_o)(z_o - z_i))\exp\left(\frac{\kappa}{2}\left(\frac{z_i}{\mu_o} + \frac{z_o}{\mu_i}\right)\right) A(\boldsymbol{r_i}, \boldsymbol{r_o})\mathrm{d}\boldsymbol{r_i}\mathrm{d}\boldsymbol{r_o} \tag{18}$$

Once again, the scattering properties of each particle that plays a role in the $n-$th order scattering is explicitly involved through the varying phase function. The use of a constant phase function $p(\Theta) = p$ brings back to the isotropic case already discussed in Section 3.5.

Finally, the cyclical term contributes to the complete appearance of the dry powder through the partial BRDF:

$$BRDF_C = \frac{4\pi r^2 C}{a\mu_i\mu_o} \tag{19}$$

Under the *Diffusion approximation*, the multiple scattering terms 16 and 19 are reduced to the analytical formulas given by the Eqs. 9. By extending the work from [17] the parameters involved in the model are defined such as in Eqs. 10 so that the model is valid for any geometry including various incident directions, but using $\kappa_{tr} = 1 - \rho g$ to also account for the phase function anisotropy in the multiple scattering.

5.2. Surface scattering

In our model, surface scattering is reduced to the specular contribution. The light that is incoming on a rough surface such as the interface between air and a dry powder is scattered in a lobe around the specular direction.

Two options have been considered to include such a phenomenon in our model. The former is to model the specular peak by a gaussian function. According to the measurements performed in Section 4 the specular scattering is very weak so this simple method is reliable enough to reproduce the specular contribution of dry powders, although it is empirical. By assuming a uniform distribution of the surface normals, it requires only one parameter which is the gaussian half width σ. With this modeling the surface scattering BRDF is written as:

$$BRDF_s = \frac{1}{\sigma\sqrt{2\pi}}\exp(\frac{-\Theta^2}{2\sigma^2}) \tag{20}$$

The second option, which is the one we chose to use, relies on the physical approach from Harvey-Shack [6] that accounts for diffraction effects caused by the surface asperities. Using this theory, the incoming light on a rough surface is then scattered around the specular direction according to the following BRDF:

$$BRDF_s = \frac{4\pi^2}{\lambda^4}(\cos\theta_i + \cos\theta_o)^2 PSD(\mathbf{f}) \tag{21}$$

where the power spread function (PSD) models a rough surface topography. We chose a gaussian power spread function, involving a roughness parameter σ_s and a correlation length l_c that quantifies the mean distance for which the surface roughness of two points on the surface are completely independent.

$$PSD(\mathbf{f}) = \pi\sigma_s^2 l_c^2 \exp(-\pi^2 l_c^2 (f_x^2 + f_y^2)) \tag{22}$$

5.3. Complete model

Our complete model is the weighted sum of volume and surface contributions according to Eq. 12 respectively given by the adapted enhanced back scattering model and a specular model. Note that the roughness parameter involved in the surface contribution has been included in the amplitude parameter $A'_s = A_s\sigma_s^2$ in order to reduce the number of optimization parameters.

$$BRDF = A_v[BRDF_{\mathcal{L}_1}(g) + BRDF_{\mathcal{L}_{2+}}(g) + BRDF_C(g,\kappa)] + A'_s BRDF_s(l_c) \tag{23}$$

The model depends on a total of 5 empirical and physical parameters to accurately simulate the BRDF of dry powder. As it is shown in the Section 6, our model works even better while including another physical parameter to refine which is the *effective radius* of the grains, defined as the mean size of the grains actually seen by the incoming light and therefore responsible for the scattering. The influence of such parameter is shown on Figure 7. The parameters involved in our model are summarized in Table 1.

Volume scattering	
A_v	Intensity of volume scattering
g	Scattering anisotropy
κ	Extinction rate
r	effective radius (optional)
Surface scattering	
A'_s	Intensity of surface scattering
l_c	Correlation length

Table 1. Parameters involved in our BRDF model. The model can be optimized by refining only 5 parameters while the grain radius r is fixed, or by refining 6 parameters including the same 5 previous ones and an effective radius.

6. Results

In order to check on the ability of the model to simulate the pigments' BRDF, we applied it to the hematite powders measurements by optimizing the variable parameters of Table 1. We used the least squares method to fit the measurement data. A first option is to optimize while using a fixed radius. The average dimensions of the grains of a sample is deduced from SEM images and reduced to only one dimensional parameter by computing the radius of a sphere that is equivalent to the grain. To better account for the shape anisotropy this radius is computed so that the ratio of the surface over the volume of the equivalent sphere and of the grain remains constant. The final mean radius is obtained by averaging on the radii of multiple grains that are in the field of view of a single SEM image. However, in the following we chose to optimize on the grains' effective radius as it leads to better results. Indeed it allows a nicer modeling of the back scattering peak amplitude, while keeping values pretty close to the radius deduced from microscopy observations (see Table 2). The comparison of the two optimizations performed on sample 2 is shown on Figure 7. The optimization is performed for all geometries of incidence whose back scattering contribution has been measured, which corresponds to incidence smaller than 60°. We only account for the measurements at the wavelength 700nm, the spectral dependency of the model being discuss later on.

For comparison, the same optimization process is performed using both Spectralon and RTLSR models adapted to be relevant in the case of dry powders. Such adaptations to the original models are detailed in Supplemental work. Results of the optimization process for the sample 1 are given on the Figures 8, 9, and 10. The results obtained for other samples are listed in Supplementary work.

Our model is able to reproduce the measured BRDF of hematite powders with an accuracy comparable to that of the Spectralon mode ($< 8\%$ of the reflectance factor), but with a much lower

complexity: only 6 parameters related to physical properties of the samples are required against 12 empirical ones for the Spectralon's model. It is particularly efficient in the case of samples whose morphology is easily characterized, that is to say for the samples with well-crystallized single-crystals. Both the back-scattering and the specular contributions are detected and modeled, even thought the latter is sometimes too weak for the modeling to be reliable. Errors are mostly spotted around the back scattering peak because of the measurements' poor sampling and interpolation at these geometries. Let's note that we have encountered difficulties in the modelization of samples 3 and C's BRDFs that we attributed to the more complex morphology of these powders. These powders are note monodisperse since they show two size populations and agglomerations of grains. An extension of our model is proposed in supplementary work to deal with powders presenting two grain size populations.

Sample	Radius SEM (nm)	Effective radius (nm)		
1	13 ± 3.0	17		
2	12 ± 1.6	16		
3	22 ± 3.7	16		
4	25 ± 4.1	15		
Sample	Large radius SEM (nm)	Effective radius (nm)	Small radius SEM (nm)	Effective radius (nm)
5	83 ± 34	83	47 ± 5.3	46
6	687 ± 64.0	687	10 ± 0.4	43
7	2222 ± 1054	2222	49 ± 13	49

Table 2. Comparison of the radius deduced from SEM observations and the effective radius obtained by the optimization of our model. For samples 5 to 7, the model extension for two size populations presented in Supplementary work is used. As it takes two different radii to optimize, two effective radii are obtained.

Since the refined parameters permit our model to quite precisely fit with the measurements in any geometry, it appears that none of them depends on the incoming, outgoing and azimuthal directions. The model is then able to predict the appearance of the studied powder in any other geometry that hasn't been considered during its optimization. The results are convenient even for more grazing angles such as incidence $\theta_i = 60°$ as shown on Figure 7.

7. Discussion & Conclusion

From BRDF measurements, we highlighted that in the particular case of dry powders the light is mainly back scattered. We proposed a new BRDF model accounting for three different scattering interactions: single scattering, incoherent multiple scattering and coherent multiple scattering responsible for the sharp peak in the backward direction. It is a semi-empirical and analytical model based on the propagation of light inside a granular medium that involves the physico-chemical properties of the powders connected only six refinement parameters.

The model has been validated against the BRDF measurements of seven $\alpha - Fe_2O_3$ hematite powders, and compared to two adapted existing models. Ours is able to reproduce the measured BRDF with an accuracy comparable to the one of the Spectralon's model, but with a much lower complexity. It can be used in its original form to reproduce the appearance of a mono

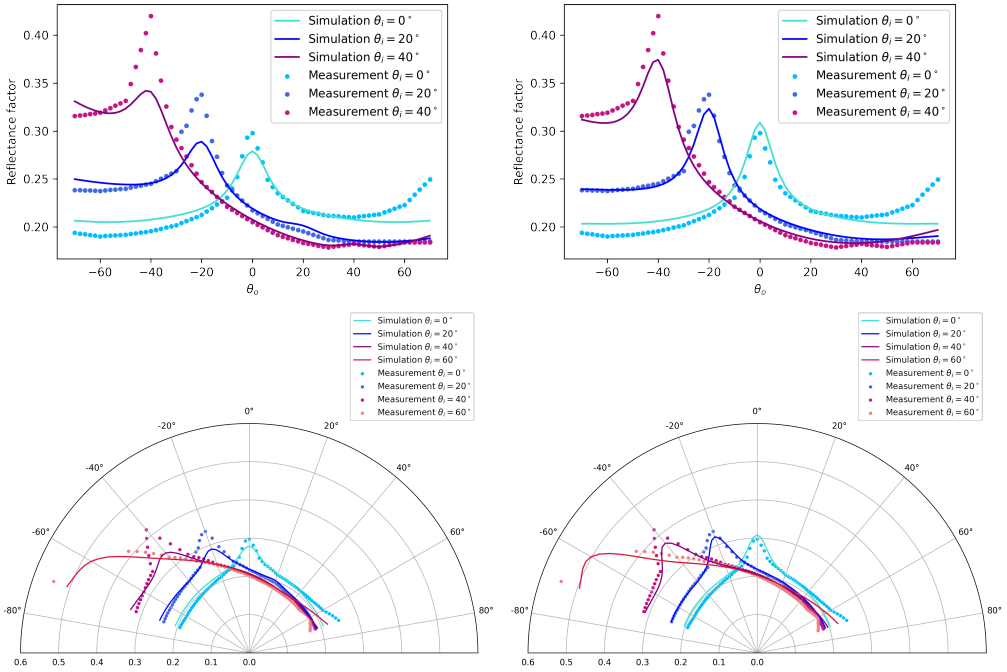

(a) Fixed radius $r = 12.5$ nm.

(b) Effective radius $r = 16.4$ nm.

Fig. 7. Influence of the grain radius optimization on the results of sample 2, in the incident plane ($\varphi = 0°$) for incidences $\theta_i = 0°, 20°$ and $40°$. The effective radius found by optimization ($r = 16.4$ nm) is pretty close to the theoretical result deduced from SEM observations ($r = 12.5$ nm). On the polar representation, the prediction of our model for incidence $\theta_i = 60°$ is also given.

disperse powder with spherical grains, or in its extended form presented in Supplementary work to account for more complex morphology involving multiple grains size populations.

Our model still has some limitations. The results obtained for specular scattering are quite questionable since the specular contribution is very weak and almost unnoticeable on the BRDF measurements. A more accurate model should be established by studying powders showing shiny and sparkling reflections such as eye shadow.

More generally, the model is not able to predict the appearance of any powder whose BRDF has not been measured beforehand. This would require to establish a relationship between the variable parameters of the model and the physico-chemical parameters of the material the powder is composed of, which requires to study much more samples with more variability in sizes.

The validity of the model's wavelength dependency is also a main issue that couldn't be solved throughout this work. At smaller wavelengths, the optimization is not robust enough to lead to nice fitting results (see Figure 11). This might be caused by a poor knowledge of the optical constants of the studied material which is the only fixed parameter known as spectrally varying. Indeed, it is mainly described by the optical constant at stake whose value appears to be quite doubtful according to the discrepancies between the results in the literature [30, 31]. Such uncertainties are often ignored in both material science and computer graphics whereas it surely affects the results.

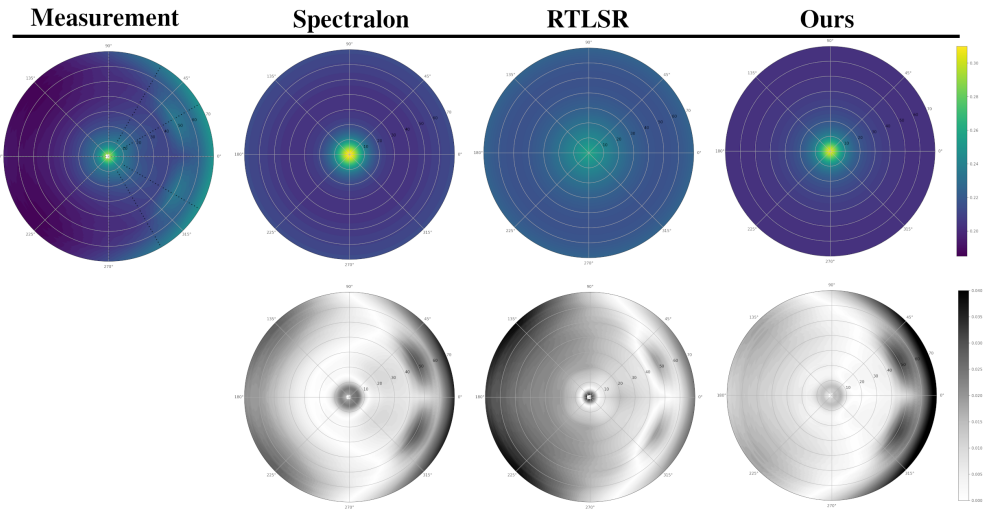

Fig. 8. Upper raw: Simulation of sample 1's BRDF using our model, spectralon and RTLSR models adapted to dry powders, at incidence $\theta_i = 0°$. Lower raw: difference between the measurement and the simulation.

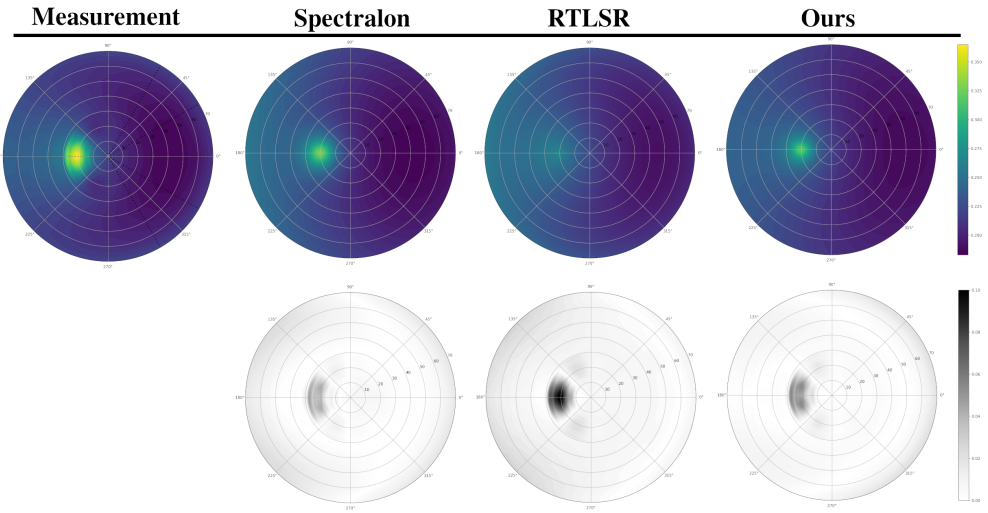

Fig. 9. Upper raw: Simulation of sample 1's BRDF using our model, spectralon and RTLSR models adapted to dry powders, at incidence $\theta_i = 20°$. Lower raw: difference between the measurement and the simulation.

As a future work we would like to implement our dry powder BRDF model in a physically based renderer so that photo-realistic renderings of the powders can be made. This would first allow the validation of the model by comparing the rendered image with photographs of the actual samples. It would also permit, by letting the user choose the values of the variable parameters to either reproduce the appearance of other powder materials, or to create new ones.

Although the model has been tested for only one material, we believe it can be used for any other pure pigment. In the case of parietal paintings, ochers (mixture of one iron-based coloring

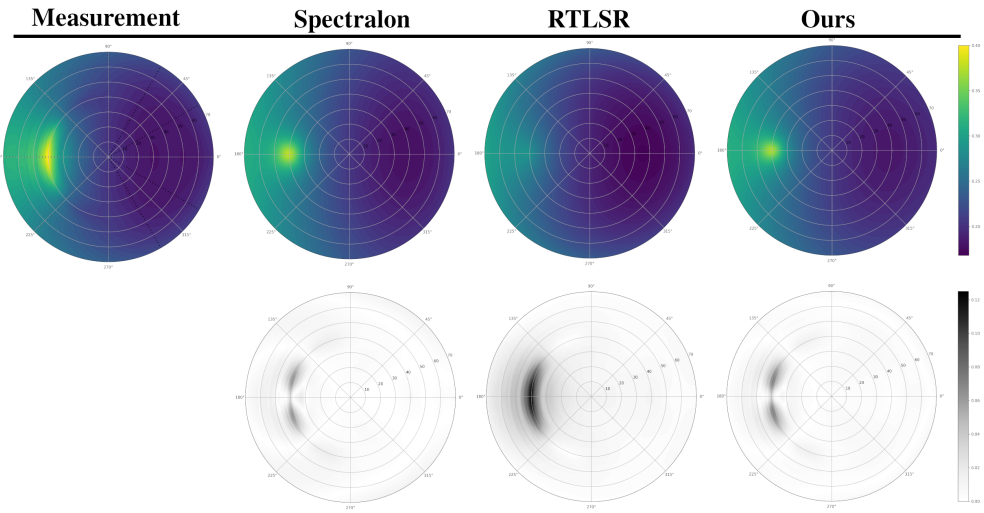

Fig. 10. Upper raw: Simulation of sample 1's BRDF using our model, spectralon and RTLSR models adapted to dry powders, at incidence $\theta_i = 40°$. Lower raw: difference between the measurement and the simulation.

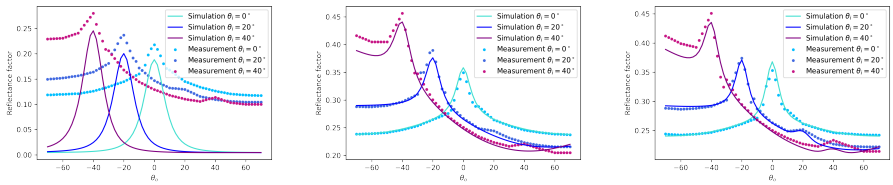

(a) At wavelength 600 nm. (b) At wavelength 700 nm. (c) At wavelength 800 nm

Fig. 11. Optimization of our model at different wavelengths using the optical constants from [30]. For smaller wavelengths, our model is not able to accurately fit the measurements.

pigment and colorless powders such as clays) and mixtures of different pigments were more commonly used than pure and almost pure iron oxide. In order to reproduce photo-realistic appearance of such paintings, we would like to extend our model to more complex powders.

The assumption of optically thick layer of powder is also too restrictive. An extension of the enhanced back scattering theory for thin films and isotropic scatterers has been proposed by [18] and may be a good starting point for our model adaptation, leading to a better reproduction of the appearance of painting layers.

Acknowledgments. The authors would like to thank Alain Ibanez and Simon Giraud (Institut Néel) for the hematite samples syntheses. Our thanks also go to Corinne Félix (Institut Néel) for her help in developing the back-scattering measurement device, as well as Bernard Schmitt and Olivier Brissaud (IPAG) for their help in the reflectance measurements using SHADOWS gonio-spectro-photometer. This work was financially supported by the French National Research Agency in the framework of the Investissements d'Avenir program (ANR-15-IDEX-02, Cross Disciplinary Program Patrimalp).

Supplemental document. See Supplement 1 for supporting content.

References

1. E. Chalmin, M. Menu, M.-P. Pomiès, C. Vignaud, N. Aujoulat, and J.-M. Geneste, "Les blasons de lascaux," L'anthropologie **108**, 571–592 (2004).
2. M. Gerardin, N. Holzschuch, A. Ibanez, B. Schmitt, and P. Martinetto, "Influence of micro-structural features on the colour of nanocrystallised powders of hematite and visible-nir reflectance spectra simulations," J. international colour association **26**, 41–48 (2021).
3. J. R. Frisvad, N. J. Christensen, and H. W. Jensen, "Computing the scattering properties of participating media using lorenz-mie theory," in *ACM SIGGRAPH 2007 papers,* (2007), pp. 60–es.
4. C. F. Bohren and D. R. Huffman, *Absorption and scattering of light by small particles* (John Wiley & Sons, 2008).
5. R. L. Cook and K. E. Torrance, "A reflectance model for computer graphics," ACM Transactions on Graph. (ToG) **1**, 7–24 (1982).
6. A. Krywonos, "Predicting surface scatter using a linear systems formulation of non-paraxial scalar diffraction" (2006).
7. P. Beck, A. Pommerol, N. Thomas, B. Schmitt, F. Moynier, and J.-A. Barrat, "Photometry of meteorites," Icarus **218**, 364–377 (2012).
8. M. Lévesque and M. Dissanka, "Measurement and modeling of the spectralon spectro-polarimetric bidirectional reflectance distribution function (brdf)" (2016).
9. J.-L. Roujean, M. Leroy, and P.-Y. Deschamps, "A bidirectional reflectance model of the earth's surface for the correction of remote sensing data," J. Geophys. Res. Atmospheres **97**, 20455–20468 (1992).
10. W. Lucht, C. B. Schaaf, and A. H. Strahler, "An algorithm for the retrieval of albedo from space using semiempirical brdf models," IEEE Transactions on Geosci. Remote. sensing **38**, 977–998 (2000).
11. J. Ross, "The radiation regime and architecture of plant stands. the hague: Dr. w," Junk Publ. doi **10**, 978–94 (1981).
12. X. Li and A. H. Strahler, "Geometric-optical bidirectional reflectance modeling of a conifer forest canopy," IEEE Transactions on Geosci. Remote. Sens. pp. 906–919 (1986).
13. W. Wanner, X. Li, and A. Strahler, "On the derivation of kernels for kernel-driven models of bidirectional reflectance," J. Geophys. Res. Atmospheres **100**, 21077–21089 (1995).
14. Z. Jiao, A. Ding, A. Kokhanovsky, C. Schaaf, F.-M. Bréon, Y. Dong, Z. Wang, Y. Liu, X. Zhang, S. Yin *et al.*, "Development of a snow kernel to better model the anisotropic reflectance of pure snow in a kernel-driven brdf model framework," Remote. sensing environment **221**, 198–209 (2019).
15. T. Nilson and A. Kuusk, "A reflectance model for the homogeneous plant canopy and its inversion," Remote. Sens. Environ. **27**, 157–167 (1989).
16. W. Ni, X. Li, C. E. Woodcock, M. R. Caetano, and A. H. Strahler, "An analytical hybrid gort model for bidirectional reflectance over discontinuous plant canopies," IEEE Transactions on Geosci. Remote. Sens. **37**, 987–999 (1999).
17. L. Tsang and J. A. Kong, *Scattering of electromagnetic waves: advanced topics*, vol. 26 (John Wiley & Sons, 2004).
18. M. B. Van Der Mark, M. P. van Albada, and A. Lagendijk, "Light scattering in strongly scattering media: multiple scattering and weak localization," Phys. Rev. B **37**, 3575 (1988).
19. S. Chandrasekhar, *Radiative transfer* (Courier Corporation, 2013).
20. A. Ishimaru, *Wave propagation and scattering in random media*, vol. 2 (Academic press New York, 1978).
21. L. L. Foldy, "The multiple scattering of waves. i. general theory of isotropic scattering by randomly distributed scatterers," Phys. review **67**, 107 (1945).
22. B. Bret, "Multiple light scattering in porous gallium phosphide," Ph.D. thesis, Universiteit Twente (2005).
23. S. Lönn and D. Kroon, "Utilizing enhanced backscattering for determination of scattering properties in turbid media," Lund Reports At. Phys. (2011).
24. J. Zhu, D. Pine, and D. Weitz, "Internal reflection of diffusive light in random media," Phys. Rev. A **44**, 3948 (1991).
25. M. Born and E. Wolf, *Principles of optics: electromagnetic theory of propagation, interference and diffraction of light* (Elsevier, 2013).
26. U. Schwertmann and R. M. Cornell, *Iron oxides in the laboratory: preparation and characterization* (John Wiley & Sons, 2008).
27. T. Sugimoto, A. Muramatsu, K. Sakata, and D. Shindo, "Characterization of hematite particles of different shapes," J. colloid interface science **158**, 420–428 (1993).
28. S. Potin, O. Brissaud, P. Beck, B. Schmitt, Y. Magnard, J.-J. Correia, P. Rabou, and L. Jocou, "Shadows: a spectro-gonio radiometer for bidirectional reflectance studies of dark meteorites and terrestrial analogs: design, calibrations, and performances on challenging surfaces," Appl. optics **57**, 8279–8296 (2018).
29. L. Belcour, R. Pacanowski, M. Delahaie, A. Laville-Geay, and L. Eupherte, "Bidirectional reflectance distribution function measurements and analysis of retroreflective materials," JOSA A **31**, 2561–2572 (2014).
30. M. R. Querry, "Optical constants," Tech. rep., Missouri Univ-Kansas City (1985).
31. A. H. M. J. Triaud, "Refractive indices of hematite," http://eodg.atm.ox.ac.uk/ARIA/data?Minerals/Hematite/(Triaud_2005)/hematite_Triaud_2005.ri.